



Defense Threat Reduction Agency  
8725 John J. Kingman Road, MS  
6201 Fort Belvoir, VA 22060-6201



DTRA-TR-22-18

# TECHNICAL REPORT

## Radiation Characterization of STT-RAM Devices

Distribution Statement A. Approved for public release; distribution is unlimited.

January 2022

HDTRA1-16-1-0025

Prepared by: Nader  
Bagherzadeh

University of  
California, Irvine  
Irvine, CA 92617

# REPORT DOCUMENTATION PAGE

PLEASE DO NOT RETURN YOUR FORM TO THE ABOVE ORGANIZATION.

<b>1. REPORT DATE</b> 04-01-2022	<b>2. REPORT TYPE</b> Final	<b>3. DATES COVERED</b>	
		<b>START DATE</b> February 25, 2016	<b>END DATE</b> August 31, 2021

**4. TITLE AND SUBTITLE**  
Radiation Characterization of STT-RAM Devices

<b>5a. CONTRACT NUMBER</b> HDTRA1-16-1-0025	<b>5b. GRANT NUMBER</b> HDTRA1-16-1-0025	<b>5c. PROGRAM ELEMENT NUMBER</b>
--	---	-----------------------------------

<b>5d. PROJECT NUMBER</b> J9BAP619209	<b>5e. TASK NUMBER</b>	<b>5f. WORK UNIT NUMBER</b>
--	------------------------	-----------------------------

**6. AUTHOR(S)**  
Bagherzadeh, Nader  
Davood Ozdal

**7. PERFORMING ORGANIZATION NAME(S) AND ADDRESS(ES)**  
UNIVERSITY OF CALIFORNIA, IRVINE  
141 INNOVATION DR STE 250  
IRVINE CA 92617-3213  
UNITED STATES OF AMERICA

**8. PERFORMING ORGANIZATION REPORT NUMBER**

**9. SPONSORING/MONITORING AGENCY NAME(S) AND ADDRESS(ES)**  
Sponsoring:  
Defense Threat Reduction Agency  
8725 John J. Kingman Road  
Fort Belvoir, VA 22060-6201

**10. SPONSOR/MONITOR'S ACRONYM(S)**  
DTRA

**11. SPONSOR/MONITOR'S REPORT NUMBER(S)**  
DTRA-TR-22-18

**12. DISTRIBUTION/AVAILABILITY STATEMENT**  
Distribution Statement A. Approved for public release; distribution is unlimited.

**13. SUPPLEMENTARY NOTES**

**14. ABSTRACT**

Studied the effect of gamma and neutron radiation on new STT-RAMs that we developed, evaluated defects and radiation induced damages on thin films that lead to variations in tunneling current, SEU and R/W rad-hard circuit. Plasmonic methods were devised for in-situ evaluation using modeling and device fabrication. Additionally, a rad-hard read/write circuit was designed to tolerate SEU and errors due to irradiation, using modeling and fabricated device parameters. As an extension of our efforts, we evaluated the effect of gamma radiation on spintronics based neurocomputers, and analyzed their defects and radiation induced damages, and measured their computation power under radiation. Experimental study demonstrated radiation hardness of Spin Torque Oscillators (STOs) both free running and with injection locking under heavy gamma radiation. Radiation hardening of the peripheral CMOS sense circuit was achieved by changing transistor dimension and gain. Improved design of optical readout scheme for arrays of MTJs. In summary, our results showed very little degradation in the characteristic of the STT-RAM under a heavy radiation regime. STT-RAM devices are well situated for space applications and other venues because of their radiation tolerance. The CMOS circuit surrounding the STT-RAM required rad-hard circuitry to mitigate any damages to the overall design.

**15. SUBJECT TERMS****16. SECURITY CLASSIFICATION OF:**

**a. REPORT**  
U

**b. ABSTRACT**  
U

**c. THIS PAGE**  
U

**17. LIMITATION OF ABSTRACT**

UU

**18. NUMBER OF PAGES**

27

**19a. NAME OF RESPONSIBLE PERSON**

Nader Bagherzadeh

**19b. PHONE NUMBER (Include area code)**

949 824-8720

**DTRA Basic Research FINAL Report**

**Please answer all sections of the document. You are welcome to use figures and tables to complement or enhance the text.**

**Grant/Award #:**

**PI Name:**

**Organization/Institution:**

**Project Title:**

**What are the major goals of the project?**

*List the major goals of the project as stated in the approved application or as approved by the agency. If the application lists milestones/target dates for important activities or phases of the project, identify these dates and show actual completion dates or the percentage of completion. Generally, the goals will not change from one reporting period to the next. However, if the awarding agency approved changes to the goals during the reporting period, list the revised goals and objectives. Also explain any significant changes in approach or methods from the agency approved application or plan.*

Detailed study of superparamagnetic MTJ under gamma irradiation, Study switching rate, TMR, and control of thermal effects (Q1-Q4)

Study spintronic based neural network in the non-radiation environment (Q1-Q4)

Characterize perpendicular MTJ operated as spin torque oscillator (STO) with and without ionization (Q2-Q5)

Measurement of optically generated electrical signals in MTJs (Q1-Q4)

Optical readout of MTJ structures based on PLDE (Q5-Q8)

Investigating the effect of optical readout on the magnetic state of MTJs (Q5-Q8)

### What was accomplished under these goals?

For this reporting period describe: 1) major activities; 2) specific objectives; 3) significant results, including major findings, developments, or conclusions (both positive and negative); and 4) key outcomes or other achievements. Include a discussion of stated goals not met. As the project progresses, the emphasis in reporting in this section should shift from reporting activities to reporting accomplishments.

The major focus of the first year's project goal was to study magnetic tunnel junctions (MTJs) not used as nonvolatile memory but rather as a building block for neuromorphic computing and the impact of ionizing radiation to such systems.

During the last 8 months of the project, we were able to accomplish our goal to perform a detailed study of superparamagnetic MTJ under gamma irradiation. Previously, we have studied the effect of gamma irradiation on magnetic tunnel junctions with perpendicular magnetic anisotropy (pMTJ). Expanding on our previous work showing the robustness of thermally stable pMTJs suitable for use in ST-MRAM to extreme doses or total ionization, we have determined that the stochastic switching in a pMTJ with superparamagnetic free layer (sMTJ) is robust to gamma irradiation. These results show that ionizing radiation has negligible impact on the transient switching dynamics of ST-MRAM. We also find that when tuned to the center of the bi-stable region, using spin transfer torque provided by a small dc current, the key properties of the sMTJ are little changed: tunneling magnetoresistance, thermally induced switching rate, and parallel (P) and anti-parallel (AP) dwell times. These results show great promise for implementation of sMTJs for radiation hard stochastic computing. Stochastic computing is preferable in situations where low power consumption is emphasized over speed. Additionally, sMTJs can be used as efficient universal random number generators for incorporating into other neuromorphic computing schemes. These results, in addition to results from the previous year, have recently been published in E. A. Montoya, et al, Sci Rep 10, 10220 (2020).

Spin torque nano-oscillators (STOs) emit microwave voltages, when they are driven by spin transfer torque, supplied by DC current injection, in a regime of sustained auto-oscillatory magnetization dynamics. The dynamics of STOs are highly nonlinear and their frequency is tunable by changes in the above threshold DC current. Additionally, STOs can synchronize their frequency to periodic electric and magnetic input signals and/or to other spin-torque nano-oscillators. Coupled network of spin-torque nano-oscillators can be used as building blocks of artificial intelligence hardware.

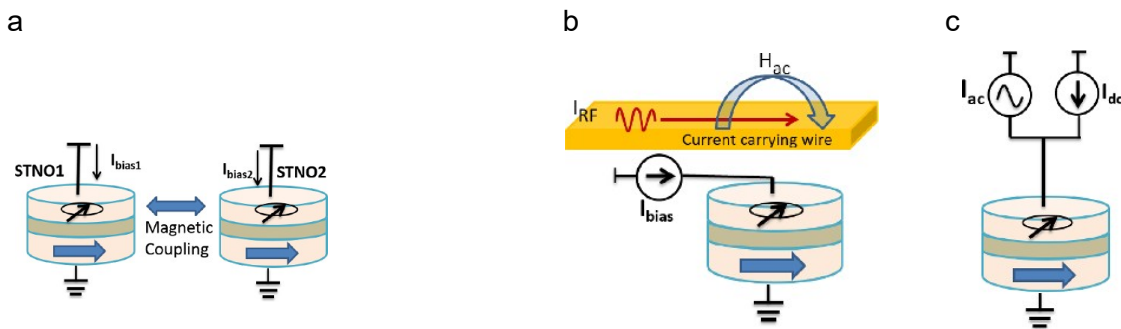


**Figure 1.** (a) Dipolar coupling of STOs. Schematic for (a) injection locking and (b) field locking of STOs to external signals. in K. Yogendra (2016). *Coupled spin torque nano-oscillators for efficient non-boolean computation*. [Doctoral dissertation, Purdue University]. ProQuest

Typically, there are two frequency locking mechanisms in the coupled STOs, self-coupling, and forced-locking/coupling mechanisms.

**Self-locking/coupling mechanism.** In self-coupling there is no external signal, and synchronization achieves through dipolar interaction between STOs' free layers or by using an electrical connection.

- Two or more STOs can interact with each other via magnetic dipolar coupling and can lock to a common frequency if they are located close to each other, as shown in Fig. 1 (a).
- Two or more STOs can also couple to each other via the current they create when they are electrically interconnected.

**Forced-locking/coupling mechanisms.** STO frequency can be locked to an external oscillating signal. If the frequency of STO is close to the frequency of injected signal, STO can be locked to that external input. The frequency-locking range depends on the type of external input and its amplitude. The injected signal can be either an oscillating current or an oscillating magnetic field.

- **Oscillating magnetic field injection.** The oscillating field ( $H_{ac}$ ) is the Oersted field generated by a wire carrying oscillating current, as shown in Fig. 1 (b).
- **Oscillating current injection.** An AC current is injected into the STO along with the DC bias, as shown in Fig. 1 (c).

We have achieved our goal of studying the STOs locking to external ac signals using LT-SPICE. We have developed the model for magnetization dynamics of perpendicular free layer MTJs including DC and AC bias and external DC and AC magnetic fields. After refining the STO SPICE model, we simulated three input locking schemes from the approaches mentioned above: Oscillating magnetic field injection with  $H_{ac}$  applied 1) in-plane and 2) perpendicular-to-plane. 3) Oscillating current injection.

The case of field injection with  $H_{ac}$  applied in-plane corresponds to the current carrying wire (stripline) positioned above or below the STO. Oscillating magnetic field injection with  $H_{ac}$  applied perpendicular-to-plane corresponds to the current carrying wire positioned adjacent to the STO. We have found that the magnetic field injection is more than an order of magnitude more efficient in the latter configuration with  $H_{ac}$  applied perpendicular to the plane. Figure 2 shows a comparison of the field locking in of these two cases. These plots show the STO output frequency  $f$  (y-axis) and amplitude (colorscale) as a function of the applied bias  $I_{dc}$  to the STO. In all figures the frequency of  $H_{ac}$  is 1.6 GHz. Fig. 2 (a) shows the case for  $H_{ac}$  applied perpendicular-to-plane with a 0.5 mT AC field. There is a small region in bias current, near  $I_{dc} = 1.2$  mA, where the natural frequency of the STO is 1.6 GHz and locking is observed. Fig. 2 (b) shows the case where  $H_{ac}$  of the same magnitude is applied in-plane. We find the locking region in bias current is greatly extended, indicating much more efficient coupling. Fig. 2 (c) shows an order of magnitude smaller input drive field applied in-plane,  $H_{ac} = 0.05$  mT. The locking region is still larger than that of Fig. 2 (a).

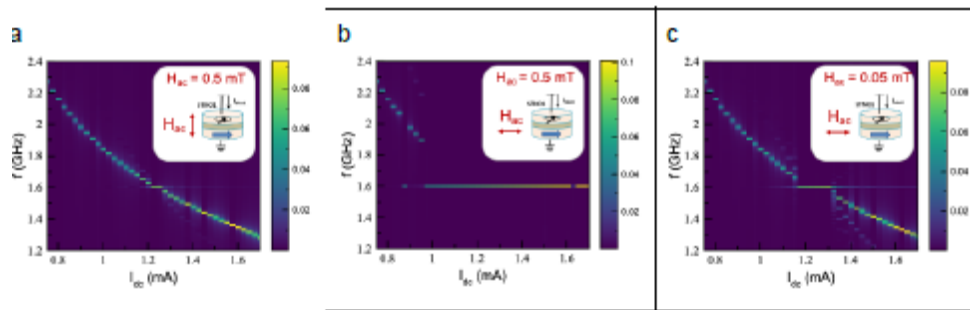


**Figure 2.** STO frequency and amplitude as a function of bias current  $I_{dc}$  for applied  $H_{ac}$  of (a) 0.5 mT perpendicular to plane, (b) 0.5 mT in-plane, and (c) 0.05 mT in-plane. We find in-plane driving field is over an order of magnitude more efficient.

As part of this study, we investigate current injection locking of single STO. Figure 3 (a) shows output frequency (y-axis) and voltage amplitude of oscillation (colorscale) of an STO biased at  $I_{dc} = 1.2$  mA as a function of the frequency of an injected AC current of  $50 \mu\text{A}$ . When the injection frequency is near the free running frequency,  $f \sim 1.6$  GHz, of the STO, the STO locks to the injection frequency.

M. Romera, et al, Nature **563**, 230 (2018) proposed that practical detection of locking of STOs in a neural network could be done via detection of the spin diode effect. In the spin diode effect, the AC current applied to the STO is rectified with the magnetoresistance (MR) oscillations and leads to a change in the DC voltage drop across the STO when the AC current and STO have the same frequency. Fig. 3 (b) shows the voltage drop across the STO as a function of AC current injection frequency. In the locking region, the magnitude of the voltage drop first decreases and then increases with increasing frequency. We find that AC injection locking leads to a phase shift between the injection current and the magnetoresistance oscillations. When the injection locking is pulling the STO frequency to a lower frequency, the AC injection current and MR oscillations are nearly inphase. When the injection current matches the free running STO frequency the phases are pi-shifted, leading to no spin diode effect. Finally, when the injection current is pushing the STO to higher frequency, the phases are nearly anti-phased leading to a spin diode effect of the opposite sign of the pulling case. We have identified that these phase effects necessitate a different detection scheme than that proposed by M. Romera et al. We also study using a small AC probe current in addition to AC field injection locking and find the phasing effects do not occur; however in this case, the magnitude of the spin diode effect is much smaller. We identify that frequency modulation is a promising future route to explore and thus it may be able to exploit the spin diode phase effects for AC current injection locking.

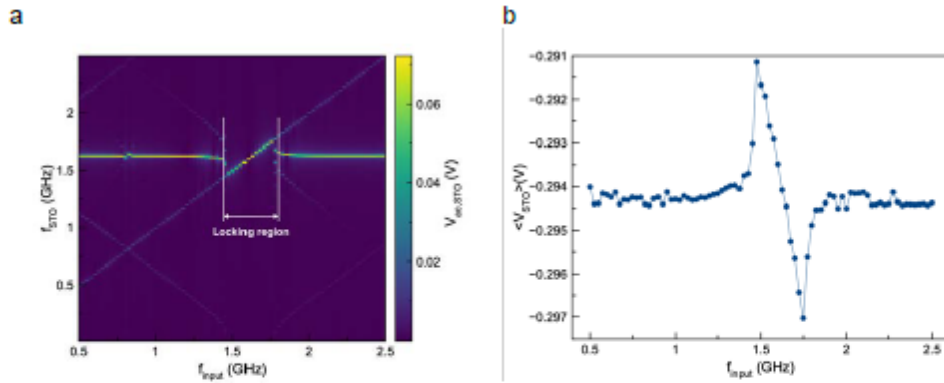


**Figure 3.** (a) AC current injection locking of STO. (B) Spin diode effect leads to change in the dsvoltage across the STO in the locking region. In the case of only using injection locking, we find the signal is anti-symmetric. In the case of field locking + AC probe current, the voltage change is symmetric.

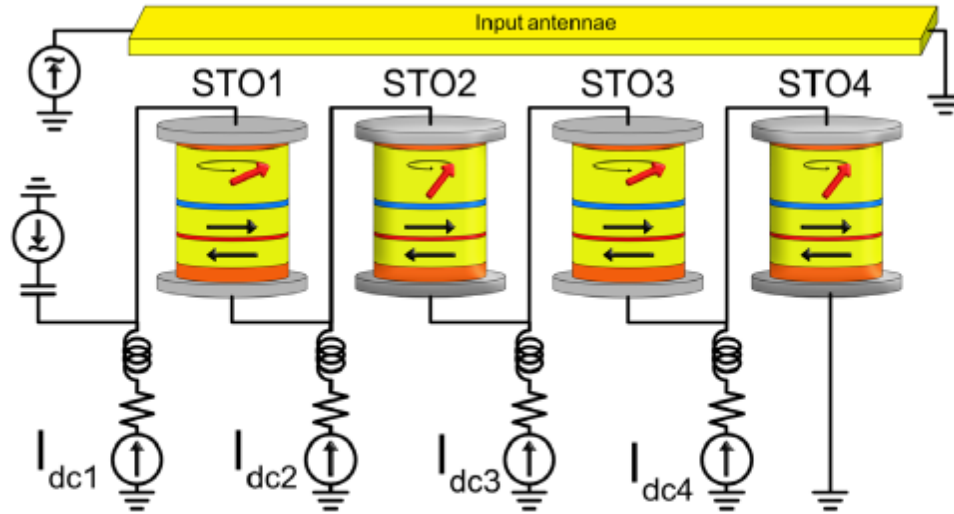


**Figure 4.** STO array capable of vowel detection. The input antennae can be used for field injections locking. The direct AC current input can be used for spin diode effect and current injection locking.

As a part of this project, we study a network of 4 STO oscillators connected in series, similar to the circuit used by M. Romera, et al for vowel detection, with the above field and current injection schemes. In this case, we study quasi-single domain free layer MTJs as opposed to vortex oscillators studied by Romera et al. An example circuit diagram is shown in Fig. 4. The circuit has been extended to allow both field injection and current injection.

Figure 5 shows example auto-oscillatory behavior for four in series STOs with 0.1 mT in-plane AC injection field with an in-phase AC probe current of 20  $\mu$ A. The four STOs are biased at 4 different values of  $I_{dc}$  such that they have different free running frequencies: STO1, STO2, STO3, and STO4 have  $I_{dc} = 1.0$  mA, 0.2 mA, 0.2 mA, and 0.2 mA, respectively. Note the total current supplied to each STO is the sum of the currents to the left. For example, the total DC bias current applied to STO2 is  $I_{dc1} + I_{dc2} = 1.2$  mA. The frequency range of the input signal is detectable by

the locking state of the STO network. We find that the 4 STO network follows similar behavior as the single STO. We find that field injection locking with a small probe AC current leads to a spin diode effect that does not change sign whether pulling or pushing the frequency, however the magnitude of the effect is smaller. This method has the advantage of simple binary detection, but with the accompanying disadvantage of smaller detectable signal. The purely AC current injection locking scheme leads to larger detectable signal, however quasi-DC binary detection is no longer possible due to phase effects. However, we identify that future designs could potentially exploit this phenomenon, where combined with frequency modulation, the locked state could be read analogous to lock-in detection.

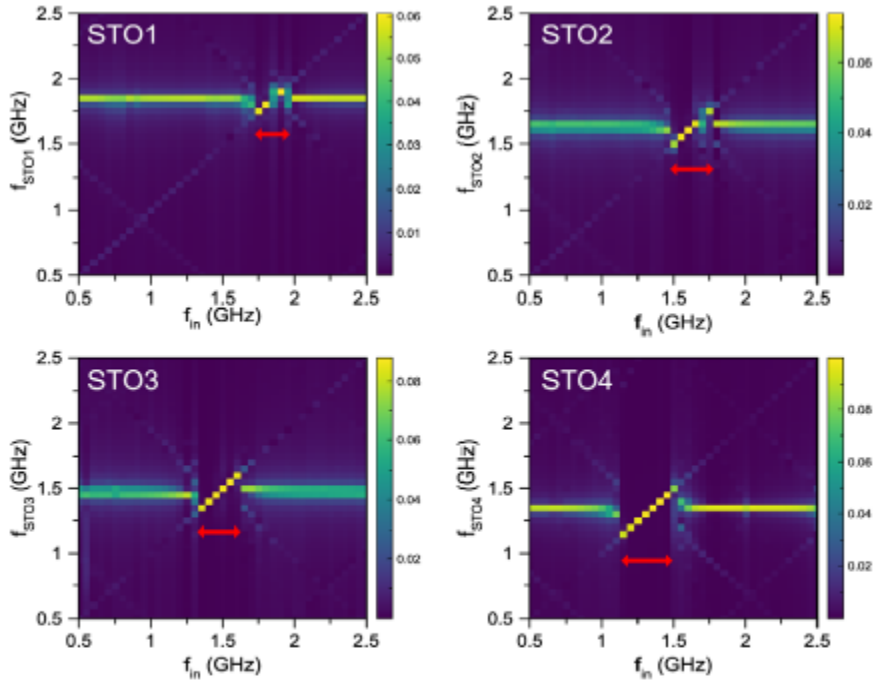


**Figure 5.** Example STO locking behavior for a 4 STO network. Each STO locks to the input signal at a different frequency range of  $f_{in}$ . Red arrows indicate the locking region for each STO.

The second step was to measure the effect of ionization on the STO model, particularly. For this purpose, the ionization effect was modeled as a pulse current and injected to the STO model. Figure 6 shows example current pulses modelled for the 22 nm technology for total charge deposited of  $Q = 1.5, 4, 12, 24,$  and  $50$  fC which corresponds to irradiation of 25, 66.7, 200, 400, and 833 krad, respectively. We find that the current pulse has negligible effect on the STO itself over a number of periods of oscillation. Therefore, we have identified that the surrounding CMOS sense circuit is the component in need of radiation hardening.

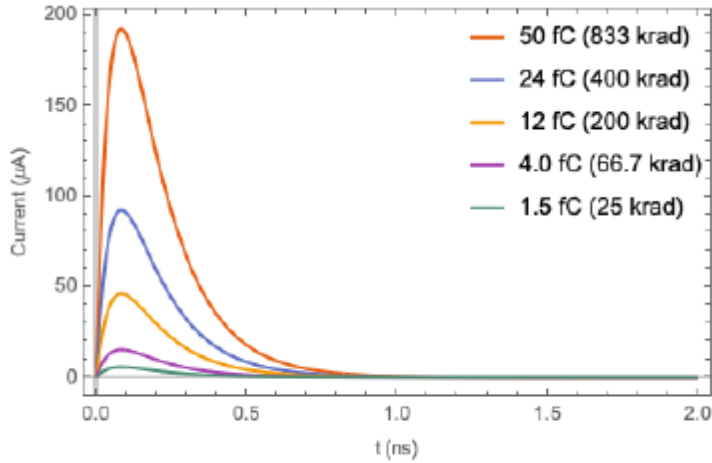
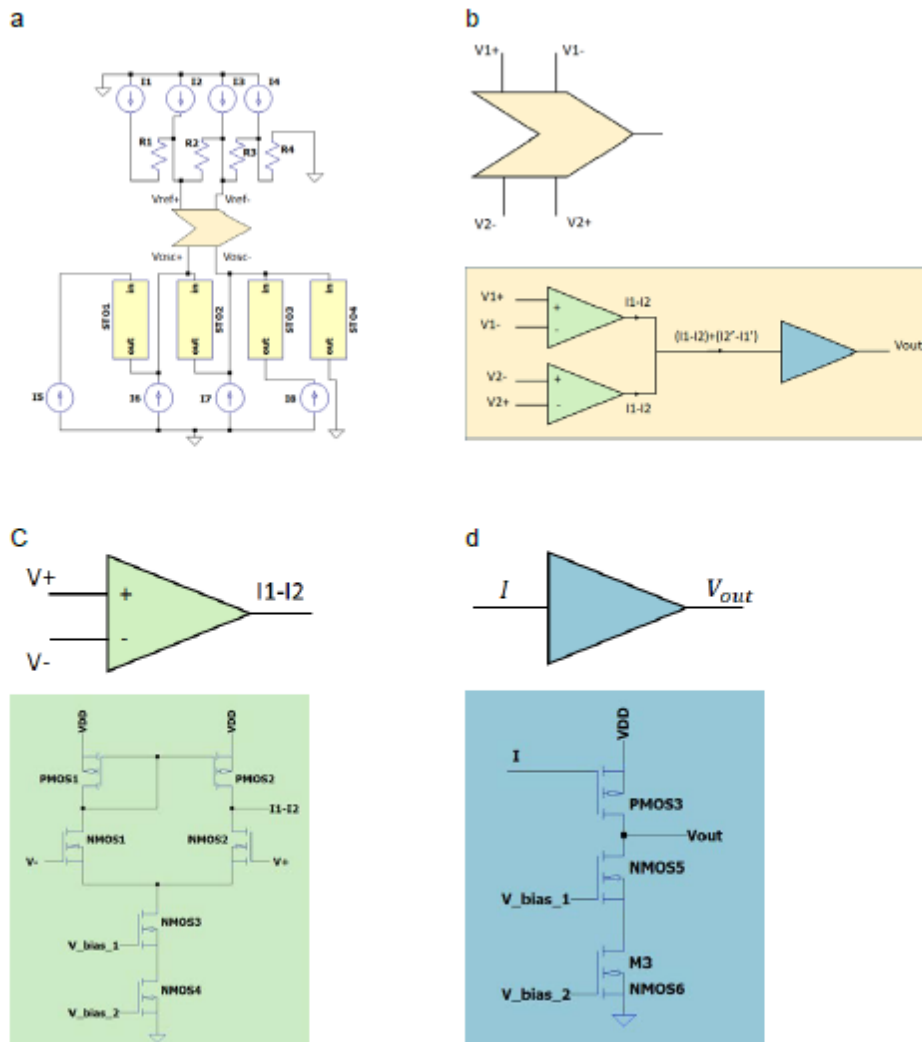


Figure 6. Radiation induced current pulse.

The detection scheme for identifying the STO locked states in the network is shown in Fig. 7a. We have adapted the detector proposed by Romera et al. for the 22 nm technology. We have used NMOS and PMOS with gate width = 45 nm and length = 100 nm. The DC voltage of each STO is compared to the voltage across a reference resistor. The comparison CMOS circuit used for detection of STO locking under the influence of AC field locking with AC current probe is pictured in Fig. 7b. It consists of two identical differential amplifiers, shown in Fig. 7c, followed by a gain stage, shown in Fig. 7d. Owing to the spin diode effect, the DC voltage drop across the STO changes in the locked state as the AC current rectifies with the AC magnetoresistance oscillations. The detection of the locking state is performed by measuring the voltage across the STO and the reference resistor, which has the same resistance as the mean resistance of the nano-oscillators, and comparing these voltages results in either of two output voltages representing the locked or unlocked state. In the locked state, the output voltage of the differential amplifier connected to the STO is lowered, as shown in the top of Fig. 8. After the gain stage, the final output is a high output voltage if STO is synchronized to the injected signal and a low output voltage otherwise.



**Figure 7.** Schematics for 4-STO network and detection of locked state. (a) STO and reference resistor comparison circuit. (b) Voltage comparing circuit using two differential amplifiers and a gain stage. (c) Differential amplifier circuit. (d) Gain stage. Circuit based on that proposed in M. Romera, et al, Nature 563, 230 (2018).

We start by applying the current pulses shown in Fig. 6 to the drain of NMOS1 in the differential amplifier. We find that the circuit is drastically impacted by large current pulses. The circuit as initially designed is robust only to smaller equivalent dose current pulses (<4.0 fC, 66.7 krad). Figure 8 shows the output of the differential amplifier detecting the STO voltage under the

influence of irradiation caused current pulses. The STO starts in the unlocked state and is put in and out of the locked state every 2 ns. One current pulse is applied at  $t = 2.2$  ns corresponding to a locked state and one is applied at  $t = 8.2$  ns corresponding to the unlocked state. Current pulses larger than 4.0 fC lead to false registers of the unlocked state. Results of further irradiation are summarized in Table 1. We have identified that the transistor gate length and width need to be adjusted to make the circuit more tolerant to large current pulses. This stage is a current work in progress.

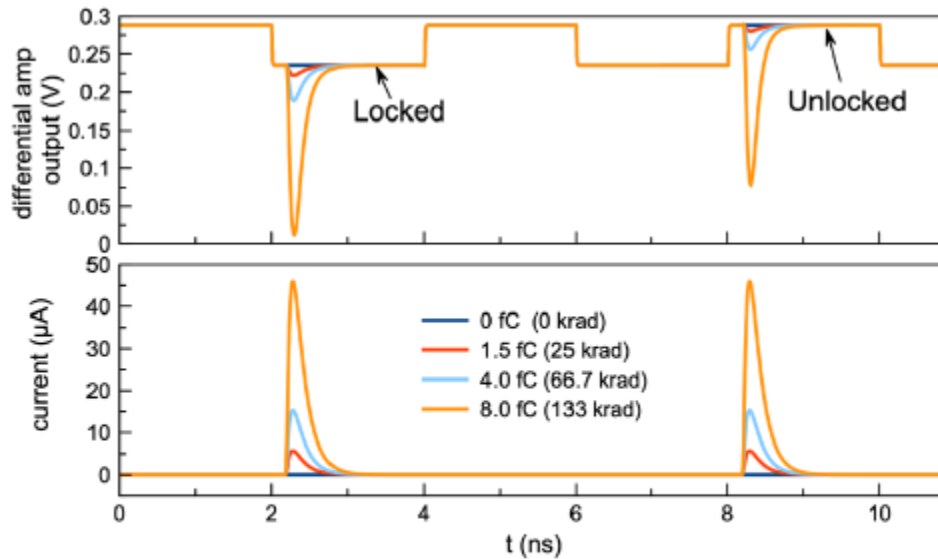


**Figure 8.** Effect of irradiation on differential amplifier output. (top) The voltage output of the differential amplifier used to detect STO locking state under the influence of current pulses applied (bottom).

Value of Q (fC)	Maximum of Current pulse (uA)	Radiation Dose Equivalent (krad)	Effect on the output
50.0	190	833	significant
24.0	91	400	significant
12.0	45	200	significant
4.0	15	66.7	moderate
1.5	5.7	25	tolerable

**Table 1.** Effect of current pulse on the sense circuit.

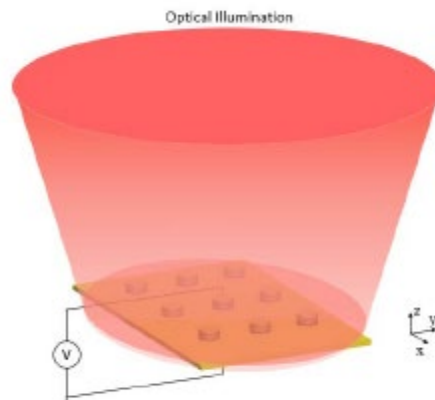


Figure 9. Optical readout scheme for an array of MTJs.

10

Another goal of the project is the measurement of optically generated electrical signals in MTJs. The plasmonic field generated on textured nano surfaces creates electrical potential in the direction perpendicular to the surface of the MTJ cells through optical rectification (OR). This phenomenon is called plasmon drag effect (PLDE), which is stronger than the so-called photon drag effect, because of its plasmonic field enhancement. Our goal here is to perform the optical readout of the MTJs by inducing such voltage in them, where the voltage is measured by conventional electronics (Fig. 9).

We note that designing the MTJ array to support a plasmonic mode highly localized in the ultrathin dielectric layer of MTJs (MgO) is important. The reason is that a change in the state of MTJ can be modeled as a change in the conductivity of MgO layer, a strong field localization in the MgO layer can contribute to the enhancement of the change in photo-induced voltage between the two states of MTJs (parallel (P) versus anti-parallel (AP)), and this leads to higher readout rates as we will discuss later in this report.

To do so, we performed simulations using COMSOL software and modeled a unit cell containing one MTJ cell with perfect electric conductor (PEC) and perfect magnetic conductor (PMC) boundary conditions to model the periodicity of the structure, to represent an array. Figure 10(a) shows the optimal geometry of the unit cell for our design, for which tuning of MTJ diameter performed to achieve optimal excitation of a localized plasmon resonance (LSPR) mode at 1.55  $\mu\text{m}$  wavelength optical illumination with normal incidence. In this design, the period of the array in both x and y directions is 50 nm (smallest gaps size due to fabrication limits) larger than the diameter of the MTJ cells, to achieve the highest possible interaction between the incident light and the MgO layer, thus enhancing the absorption. We note that the thickness of the CoFeB and MgO layers are set based on the typical thicknesses used in the literature. The field distribution of the designed LSPR mode is shown in Fig. 10(b), where one can see that the highest field localization occurs in the MgO layer, as desired for our purpose. The resonance behavior of the

designed structure can be observed in its absorption and reflection spectra shown in Fig. 10(c), as it shows an absorption peak at 1.55  $\mu\text{m}$  as well as a dip in reflection.

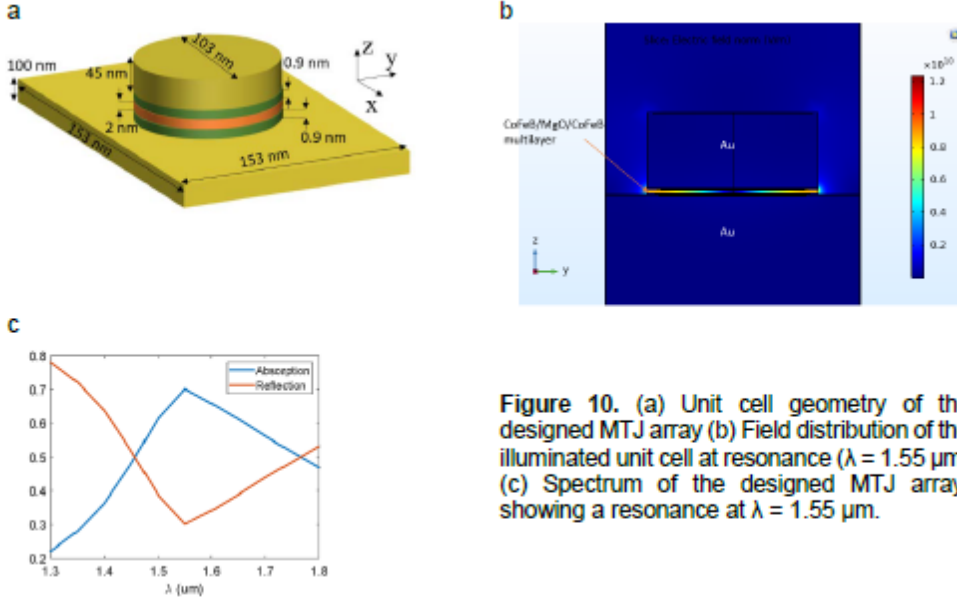


Figure 10. (a) Unit cell geometry of the designed MTJ array (b) Field distribution of the illuminated unit cell at resonance ( $\lambda = 1.55 \mu\text{m}$ ) (c) Spectrum of the designed MTJ array, showing a resonance at  $\lambda = 1.55 \mu\text{m}$ .

For calculation of the photo-induced voltage in MTJs, we adopt a general theoretical model based on the Euler's equation of fluid motion for calculation of OR effect in an array of MTJs, using the following formula provided in [1]:

$$V_{\omega-\omega,z}^{(2)} \approx \frac{1}{n^{(0)}q} \int \frac{dz}{A_z(z)} \left[ \int dA_z \cdot \left( \frac{\alpha_R}{4} \nabla |\tilde{E}(z)|^2 \right) + \frac{|\alpha|}{4} |\tilde{E}(z^-)_\perp|^2 \hat{n}(z) \cdot \hat{z} \right] \quad (1)$$

where  $V_{\omega-\omega,z}^{(2)}$  is the photo-induced voltage caused by OR along z direction (perpendicular to the surface of the MTJ cells),  $n^{(0)}$  is the zeroth-order charge density in the metal layers,  $q$  is the electron charge ( $=1.6 \times 10^{-19}$  C),  $\alpha$  is the polarizability of the metal layers and  $\alpha_R$  is the real part of it,  $A_z(z)$  is the cross section of the metal layers in xy plane at each z location,  $\tilde{E}(z)$  is the electric field vector,  $\tilde{E}_\perp(z^-)$  is the component of electric field normal to the metal surface at a depth equal to the Thomas-Fermi screening length of the metal ( $l_{TF}$ ), and  $\hat{n}$  is an outward unit vector normal to the metal surface.

We note that simplifications are made in achieving equation (1), eliminating negligible terms from equation (25) in reference [1]. Such simplification is acceptable, since in [1], it is applied to a plasmonic nanostructure and the results match with experimental results. Furthermore, we note that in our calculations, we assumed values of  $n_0 = 1.7 \times 10^{29} \text{ m}^{-3}$  and  $l_{TF} = 0.13 \text{ nm}$  are used for CoFeB layers, which are the electron density and screening length values for Fe [2]. This assumption is acceptable, since the more common form of CoFeB used for MTJs so far is  $\text{Co}_{20}\text{Fe}_{60}\text{B}_{20}$  which mostly consists of Fe.

Using equation (1), we calculate the photo-induced voltage along z direction for the designed MTJ array, for each MTJ state (P or AP). For our calculations, we use the measured value of resistance area ( $RRRR=2.9 \Omega\mu\mu\mu\mu\mu\mu^2$  with tunnel magnetoresistance (TMR) ratio of %165) from [3]. Assuming a typical MgO thickness of 2nm, MgO conductivity in each state can be calculated as:

$$RA = 2.9 \Omega\mu\mu^2 \quad (\text{for P state}) \quad t_{MgO} = 2 \text{ nm} \Rightarrow \sigma_P \approx 690 \text{ S.m}^{-1}$$

$$TMR = \%165 = 1.65 = (\sigma_P - \sigma_{AP})/\sigma_{AP} \Rightarrow \sigma_P \approx 260 \text{ S.m}^{-1}$$

We use these values as conductivity of the MgO layer for each MTJ state in our optical simulations. Having the results of the optical simulations, we define several cut planes throughout the structure of the MTJ cell and assign integration to them to calculate the photo-induced voltage for different wavelengths using equation (1). For our calculations, we use specification from a commercial laser (Chromacity OPO), with 1.7 kW peak power and 100 MHz repetition rate, and we assume the laser output is focused onto the array with spot size of  $20 \mu\text{m} \times 20 \mu\text{m}$  area. The results are presented in Fig. 11. It can be seen that the maximum voltage change between the two MTJ states is  $7.47 \mu\text{V}$  which occurs at around  $1.56 \mu\text{m}$  (close to the resonance wavelength observed in the reflection and absorption spectra).

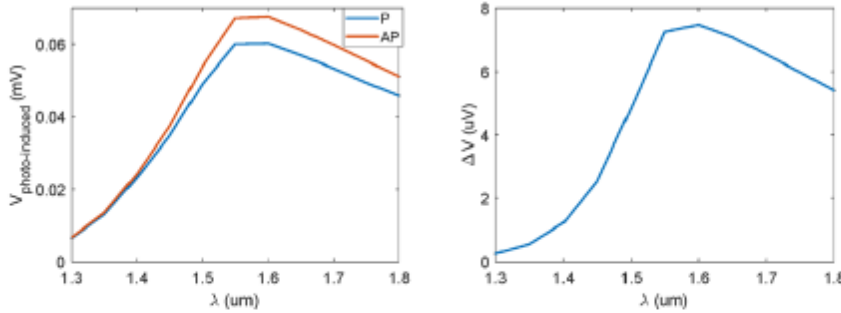


**Figure 11.** (a) Photo-induced voltage calculated assuming optical illumination of 1.7 kW power focusing onto a  $20 \mu\text{m} \times 20 \mu\text{m}$  area. (b) The difference between the photo-induced voltage of the two states ( $\Delta V = V_{AP} - V_P$ ).

To calculate the readout speed, one should first calculate the speed of electronic readout of the voltage. Assuming a commercial lock-in amplifier with noise equivalent power of  $NEP = 4nV/\sqrt{\text{Hz}}$  (Zurich Instruments UHFLI) and aiming for a signal to noise ratio of 3 dB, one can achieve a speed of approximately up to 1.74 MHz:

$$NEP * \sqrt{BW} = \frac{7.47 \mu V}{\sqrt{2}} \Rightarrow BW \approx 1.74 \text{ MHz}$$

This means that the laser repetition rate should be 1.74 MHz at its highest. Having the unit cell period of the designed MTJ array as 153 nm from our design, for an optical illumination with  $20 \mu\text{m} \times 20 \mu\text{m}$  focal spot size, approximately 17000 MTJ cells can be illuminated with each laser pulse. Therefore, the proposed scheme has the potential to provide a readout speed as high as 29.6 Gbit/sec ( $\approx 17000 \times 1.74 \text{ MHz}$ ).

During the upcoming quarter, we plan to perform studies of how the proposed optical readout method might affect the state of MTJs. In other words, we want to check how susceptible the state of MTJs can be to the proposed readout scheme. To do so, we will study the interaction between the optical illumination and the magnetization of CoFeB layers.

## References

- [1] Kurosawa, Hiroyuki, Seigo Ohno, and Kazuyuki Nakayama. "Theory of the optical-rectification effect in metallic thin films with periodic modulation." *Physical Review A* 95.3 (2017): 033844.
- [2] Zhang, Shufeng. "Spin-dependent surface screening in ferromagnets and magnetic tunnel junctions." *Physical review letters* 83.3 (1999): 640.
- [3] Ikeda, Shoji, et al. "Dependence of tunnel magnetoresistance in MgO based magnetic tunnel junctions on Ar pressure during MgO sputtering." *Japanese journal of applied physics* 44.11L (2005): L1442

One PostDoc (Eric Montoya) gained experience with SPICE simulator and modelling of spin torque oscillator networks.

One PostDoc (Eric Montoya) was invited to give invited talks at the following conferences:

- IEEE International Conference on "Nanomaterials: Applications & Properties", Odessa Ukraine, forthcoming November 2020, \* virtual due to COVID-19
- IEEE International Microwave Magnetics Conference (ICMM2020), Beijing China, June 2020. \* cancelled due to COVID-19
  - American Physical Society March Meeting, Denver CO USA, March 2020. \* cancelled due to COVID-19
  - Government Microcircuit Applications & Critical Technology Conference (GOMACTech), San Diego CA USA, March 2020. \* cancelled due to COVID-19
  - The 64th Annual Conference on Magnetism and Magnetic Materials, Las Vegas NV USA, November 2019. (symposium)

One PostDoc (Eric Montoya) was able to attend and present a poster at the 2019 IEEE International Electron Devices Meeting (IEDM), San Francisco CA USA, December 2019.

One PostDoc (Eric Montoya) was able to attend and contribute an oral presentation at the IEEE International Conference on "Nanomaterials: Applications & Properties", Odessa Ukraine, December 2019.

One PostDoc (Eric Montoya) was invited to give a virtual Condensed Matter Seminar for Simon Fraser University, April 2020.

Two PhD students (Parinaz Sadri-Moshkenani, Mohammad Wahiduzzaman Khan) gained experience regarding modeling of photo-induced voltage in plasmonic devices.

DTRA acknowledged journal papers:

1. J.-R. Chen, A. Smith, E. A. Montoya, J. G. Lu, and I. N. Krivorotov, *Spin-orbit torque nano-oscillator with giant magnetoresistance readout*, (accepted, Communications Physics 2020).
2. Smith, K. Sobotkiewich, A. Khan, E. A. Montoya, L. Yang, Z. Duan, T. Schneider, K. Lenz, J. Lindner, K. An, X. Li, and I. N. Krivorotov, *Dimensional Crossover in Spin Hall Oscillators*, Phys. Rev. B **102**, 054422 (2020).
3. P. Sadri-Moshkenani, M. W. Khan, Md. Shafiqul Islam, E. Montoya, I. Krivorotov, N. Bagherzadeh, and O. Boyraz, *Effect of Magnesium Oxide Adhesion Layer on Resonance Behavior of Plasmonic Nanostructures*, Appl. Phys. Lett. **116**, 241601 (2020).
4. E. A. Montoya, J.-R. Chen, R. Ngelale, H. K. Lee, H.-W. Tseng, L. Wan, E. Yang, P. Braganca, O. Boyraz, N. Bagherzadeh, M. Nilsson, and I. N. Krivorotov, *Immunity of Nanoscale Magnetic Tunnel Junctions with Perpendicular Magnetic Anisotropy to Ionizing Radiation*, Sci Rep **10**, 10220 (2020).
5. M. W. Khan, Q. Zhao, P. Sadri-Moshkenani, M. S. Islam, and O. Boyraz, *Graphene-Incorporated Plasmo-Thermomechanical Infrared Radiation Detection*, J. Opt. Soc. Am. B, JOSAB **37**, 774 (2020).
6. I. Barsukov, H. K. Lee, A. A. Jara, Y.-J. Chen, A. M. Gonçalves, C. Sha, J. A. Katine, R. E. Arias, B. A. Ivanov, and I. N. Krivorotov, *Giant Nonlinear Damping in Nanoscale Ferromagnets*, Science Advances **5**, eaav6943 (2019).
7. J. M. Algarín, B. Ramaswamy, Y. J. Chen, I. N. Weinberg, I. N. Krivorotov, J. A. Katine, B. Shapiro, and E. Waks, *High Rectification Sensitivity of Radiofrequency Signal through Adiabatic Stochastic Resonance in Nanoscale Magnetic Tunnel Junctions*, Appl. Phys. Lett. **115**, 192402 (2019).
8. P. Sadri-Moshkenani, M. W. Khan, M. S. Islam, I. Krivorotov, M. Nilsson, N. Bagherzadeh, and O. Boyraz, *Array of Symmetric Nanohole Dimers with High Sensitivity for Detection of Changes in an STT-RAM Ultrathin Dielectric Layer*, J. Opt. Soc. Am. B, JOSAB **36**, 3090 (2019).

DTRA acknowledged conference papers:

1. E. A. Montoya, J.-R. Chen, R. Ngelale, H. K. Lee, H.-W. Tseng, L. Wan, E. Yang, P. Braganca, O. Boyraz, N. Bagherzadeh, M. Nilsson, and I. N. Krivorotov, *Nanoscale Magnetic Tunnel Junctions for Radiation Hard STT-MRAM and Beyond*, GOMACTech (2020).
2. P. Sadri-Moshkenani, M. W. Khan, M. M. Bayer, M. S. Islam, E. Montoya, I. Krivorotov, M. Nilsson, N. Bagherzadeh, and O. Boyraz, *Effect of Tantalum and MgO adhesion layers on plasmonic nanostructures*, in Nanoengineering: Fabrication, Properties, Optics, Thin Films, and Devices XVI (International Society for Optics and Photonics, 2019), p. 1108916.

Conference and Seminar Presentations:

1. E. A. Montoya, *Magnetization reversal driven by low dimensional chaos in a nanoscale ferromagnet*, IEEE International Microwave Magnetism Conference (ICMM2020), Beijing China, June 2020. **(Invited talk)** \*COVID-19
2. E. A. Montoya, *Magnetization reversal driven by low dimensional chaos in a nanoscale ferromagnet*, American Physical Society March Meeting, Denver CO USA, March 2020. **(Invited talk)** \*COVID-19
3. E. A. Montoya, *Nanoscale Magnetic Tunnel Junctions for Radiation Hard STT-MRAM and Beyond*, Government Microcircuit Applications & Critical Technology Conference (GOMACTech), San Diego CA USA, March 2020. **(Invited talk)** \*COVID-19
4. E. A. Montoya, *A new path to magnetization switching: ac spin transfer torque driven by low dimensional chaos*, 2019 IEEE International Electron Devices Meeting (IEDM), San Francisco CA USA, December 2019. (poster)
5. E. A. Montoya, *Spin-orbit torque driven by planar Hall current*, 9th International Conference on Nanomaterials: Applications & Properties, Odessa Ukraine, September 2019. (oral)
6. E. A. Montoya, *Spin-orbit torque driven by planar Hall current*, The 64th Annual Conference on Magnetism and Magnetic Materials, Las Vegas NV USA, November 2019. **(Invited talk/symposium)**
7. E. A. Montoya, *A new path to magnetization switching: ac spin transfer torque driven by low dimensional chaos*, The 30th Magnetic Recording Conference, Minneapolis MN USA, July 2019. **(Invited talk)**
8. I. N. Krivorotov, *Novel Spin Torques*, University of California, Riverside, Riverside, CA USA, November 2019. **(Colloquium)**
9. I. N. Krivorotov, *Magnetization Reversal Driven by Chaos in a Nanoscale Ferromagnet*, Conference on Magnetism and Magnetic Materials, Las Vegas NV USA, November 2019 **(Invited Talk)**
10. I. N. Krivorotov, *Novel spin torques*, 4th Keck Energy Materials Program Symposium, Long Beach CA USA, September 2019 **(Symposium)**

## LAST YEAR ACCOMPLISHMENTS

### Radiation hardness of neuromorphic building blocks

The major focus of this last period of the project goal is to study magnetic tunnel junctions (MTJs) not used as nonvolatile memory but rather as a building block for neuromorphic computing and the impact of ionizing radiation to such systems. To this end, our goal for this last year was to study MTJs operated as spin torque oscillator (STOs). We have achieved our two main goals during this period:

1. In-situ study of STO operation in gamma ray environment.

## 2. Study of injection locking of STO in the gamma ray environment.

### In-situ study of STO in gamma ray environment

During this reporting period we have achieved our goal to characterize perpendicular MTJ operated a spin torque oscillator (STO) with and without the presence ionizing radiation. We have demonstrated the STO's robustness to gamma irradiation, demonstrating the key parameters, frequency, linewidth, and amplitude, are not impacted by ionizing radiation as described below.

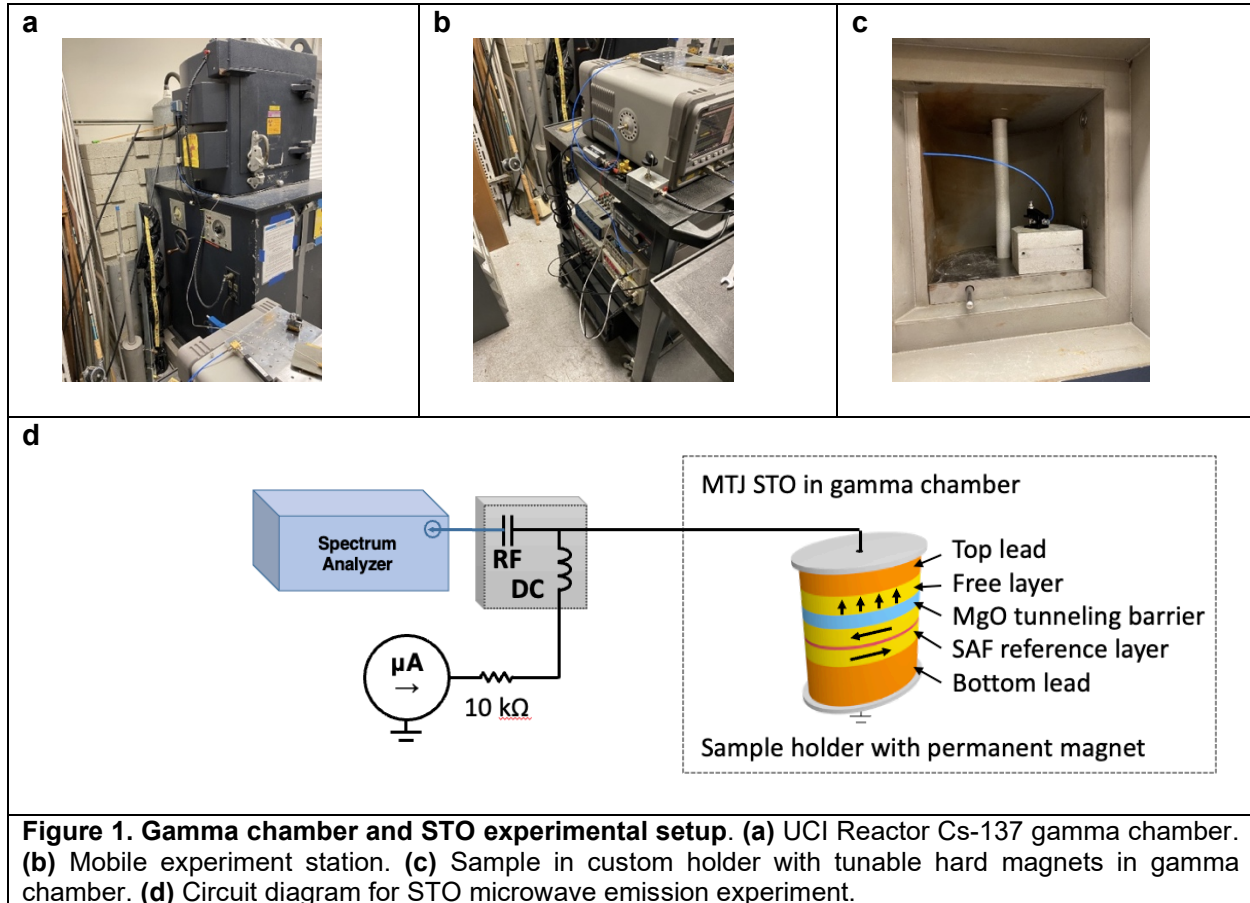


**Figure 1. Gamma chamber and STO experimental setup. (a)** UCI Reactor Cs-137 gamma chamber. **(b)** Mobile experiment station. **(c)** Sample in custom holder with tunable hard magnets in gamma chamber. **(d)** Circuit diagram for STO microwave emission experiment.

We have experimentally characterized perpendicular free layer MTJs operated as spin torque oscillators (STO) in the presence of ionization radiation. We have developed a mobile experiment station for characterization of STO emission in the UCI Reactor Cs-137 gamma chamber as shown in Figure 1 (a)-(c). We have used an  $60 \times 70 \text{ nm}^2$  elliptical MTJ with in-plane free layers and perpendicular anisotropy free layers. The sample structure is seed layer/SAF/MgO barrier/Free Layer/top layer. The bottom lead is Ta(3)/CuN(40)/Ta(3)/CuN(40)/Ta(3)/Ru(10)/Ta(5)/PtMn(15), where numbers in parenthesis are layer thickness in nm. The synthetic antiferromagnet (SAF) reference layer is  $\text{Co}_{70}\text{Fe}_{30}(2.3)/\text{Ru}(0.85)/\text{Co}_{40}\text{Fe}_{40}\text{B}_{20}$ . The top lead is Ta(5)/Cu(10)/Ru(5)/Ta(3). The magnetic free layer is  $\text{Co}_{20}\text{Fe}_{60}\text{B}_{20}(1.8)$ , which is thin enough to have net perpendicular magnetic anisotropy.

We measure microwave emission from the STO using a spectrum analyzer, as shown in Fig. 1 (d). A dc bias current  $I_{\text{dc}}$  is applied to the device via the low frequency arm of a bias tee. Above a threshold current, auto-oscillatory magnetization dynamics are induced, and the device operates as a spin torque oscillator. The dynamic magnetization leads to dynamic resistance oscillations, which by means of the TMR effect and combined with the dc bias current, lead to microwave voltage emission that is detected via spectrum analyzer connected to the high frequency arm of the bias tee.

Microwave emission results from the STO are shown in Fig. 2. The samples were placed in the gamma chamber and the emission experiment was repeated 10 times before, during, and after gamma irradiation. The dose rate for gamma irradiation was  $\sim 0.7 \text{ kGy/h}$  ( $70 \text{ krad/h}$ ) [silica]. The total ionizing dose (TID) was  $0.5 \text{ kGy}$  ( $50 \text{ krad}$ ). Example microwave emission as a function of  $I_{\text{dc}}$  before, during, and after irradiation is shown in Fig. 2 (a), (b), and (c) respectively. The frequency

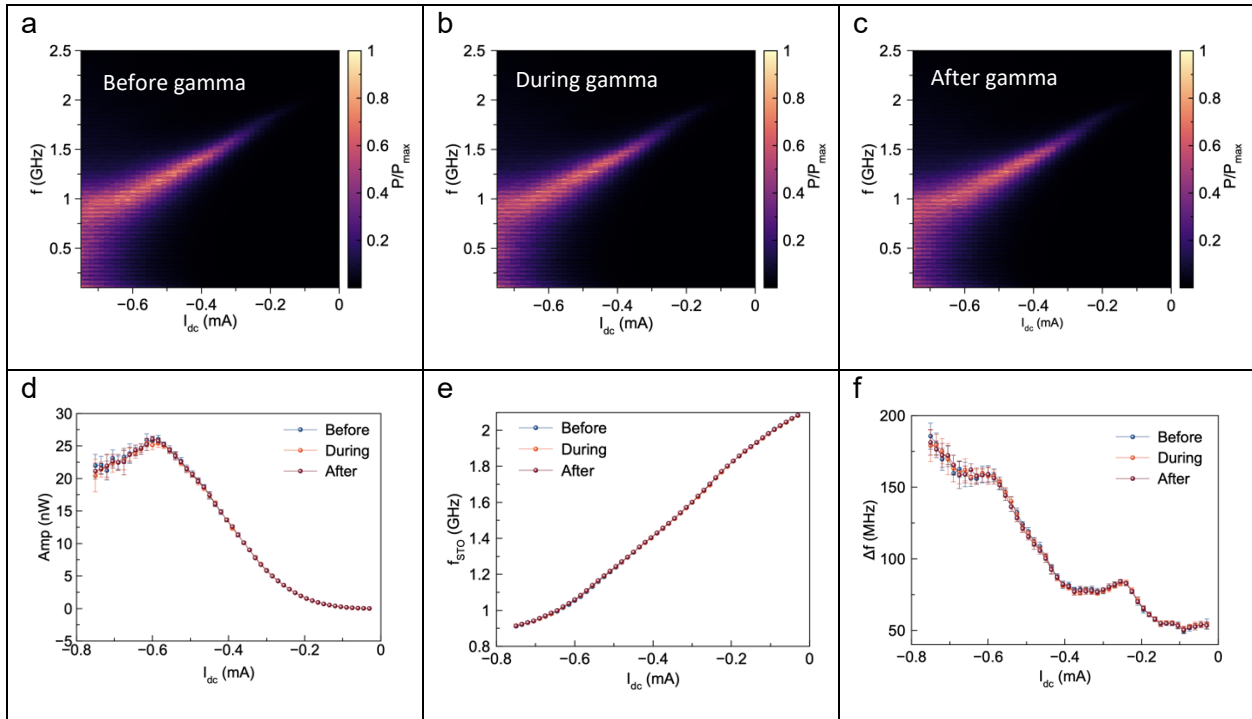


**Figure 2. Microwave emission from spin torque oscillator.** Example experimental microwave emission as a function of bias current  $I_{\text{dc}}$  for (a) before, (b) during, (c) after gamma irradiation. Note emission traces are nearly identical. Mean STO microwave emission (e) amplitude, (f) frequency, and (g) linewidth for 10 traces each taken before, during, and after gamma irradiation [error bar indicates 1 standard deviation]. These key parameters of STO operation are found to be immune to gamma irradiation.

of emission is displayed on the y-axis and the emission power is encoded in color scale. We find the STO emission is nearly identical in the presence of gamma irradiation as compared to without gamma irradiation, both before and after. Fig. 2 (d) shows the mean amplitude of microwave emission as a function of  $I_{dc}$  for 10 traces each for before, during, and after irradiation (error bars indicate 1 standard deviation), indicating the emission amplitude is robust to gamma irradiation. Fig. 2 (e) shows the results emission frequency  $f_{STO}$  as a function of  $I_{dc}$ , indicating the emission frequency is also unaffected by the gamma radiation. Finally, Fig. 2 (f) show the results of the emission linewidth as a function of  $I_{dc}$ , again demonstrating the STO is unaffected. The results shown in Fig 2 (d)-(f) demonstrate that the MTJ based STO dynamics are immune to the studied level of gamma irradiation (0.7 kGy/h (70 krad/h) [silica]).

### Study of injection locking of STO in the gamma ray environment.

In order to achieve neuromorphic computing using STOs, the STOs must be able to couple to each other and to external microwave frequency signal. To study whether or not gamma irradiation has a significant impact on STO coupling to microwave voltage signals, we studied injection locking to an external microwave signal both in and out of the presence of gamma irradiation. A schematic of the injection locking circuit is shown in Fig. 3.

For this study a number of experiments were performed sequentially and repeatedly both inside the gamma chamber and outside. The sample was the same stack structure as above but with an elliptical area of  $60 \times 190 \text{ nm}^2$ ; it was subjected to stronger gamma irradiation for a longer time in order to study both transient and total ionizing dose effects. The sample was placed closer to the gamma source for a dose rate of  $\sim 1.3 \text{ kGy/h}$  (130 krad/h) [silica]. The sample was irradiated for a total of 20.25 h, for a TID of  $\sim 26 \text{ kGy}$  (2.6 Mrad) [silica] in order to see if long term TID impacted STO operation. This TID is an order of magnitude larger than that needed for the Europa Clipper Mission [3 kGy or 300 krad].

The first experiment essentially repeated the experiment in the previous section where the free running STO was characterized. Figure 4 (a) shows the STO frequency as function of current bias  $I_{dc}$ . This measurement was repeated 5 times over the course of 2 h in the chamber before the gamma irradiation was turned on; the mean results are shown as the circles labelled “Before  $\gamma$ ”. This measurement was also performed 23 times over the course of the first 9.4 h with the gamma irradiation on, with the mean results shown as the squares labelled “During  $\gamma$ ”. Finally, the measurement was repeated 4 times of the course of 1.6 h in the chamber after the gamma irradiation was turned off, with the mean results shown as triangles labelled “After  $\gamma$ ”. The error

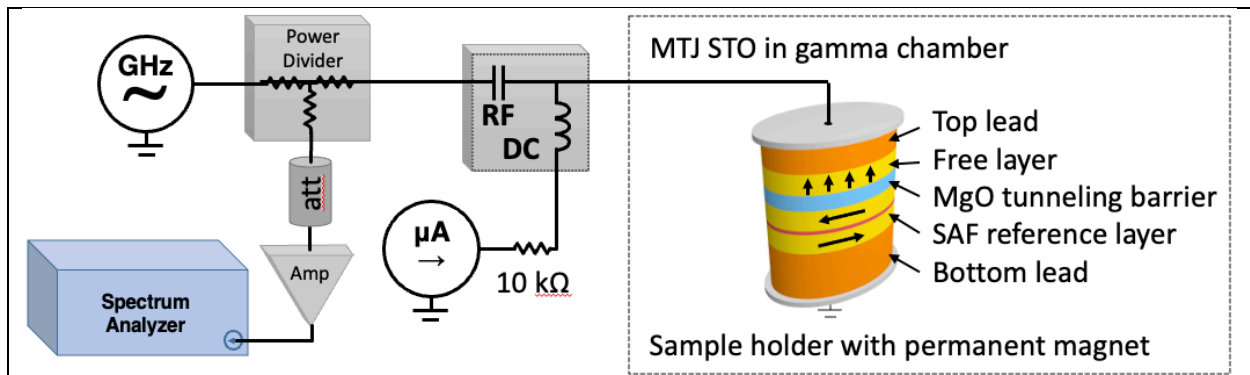
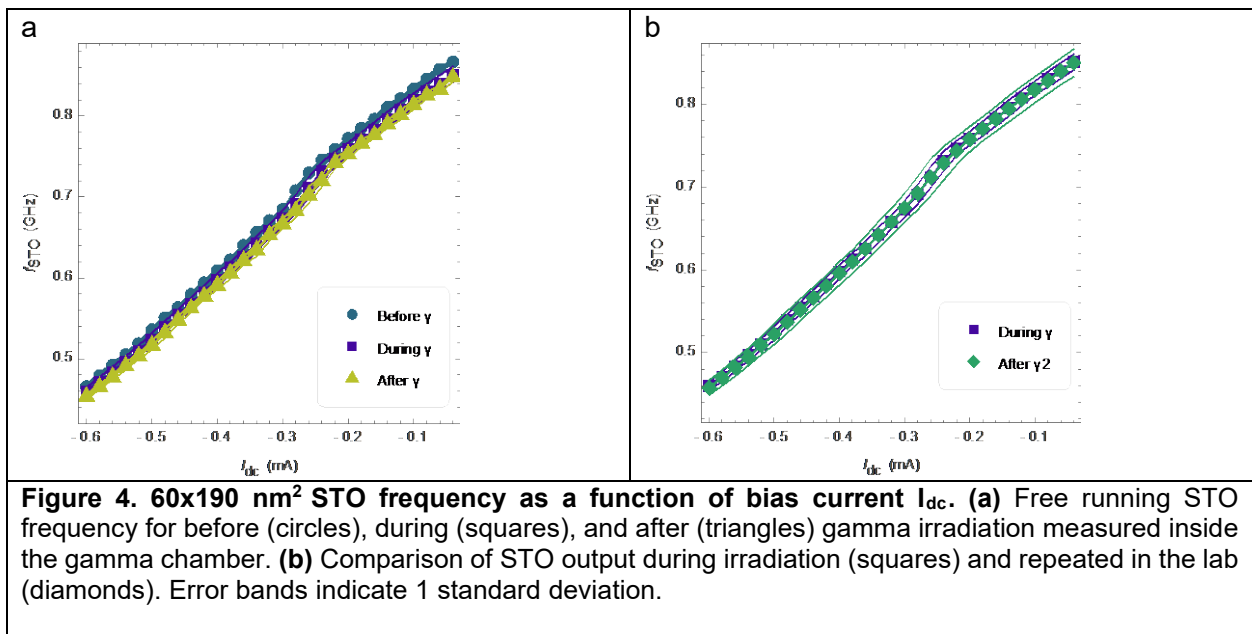


**Figure 3. Schematic of injection locking circuit.** Microwave drive is applied to the STO by means of a broadband microwave generator.



bands here indicate 1 standard deviation. Upon first inspection it seems as if this device is less robust to gamma irradiation than the device in the previous section, as it appears as though  $f_{STO}$  for a given  $I_{dc}$  is reduced over the  $\sim 26$  h from first measurement to last measurement. To see if the apparent effect is due to gamma irradiation, we repeatedly perform the same set of measurements in the lab of the course of 24 h. The results of this measurement are the diamonds labeled “After  $\gamma^2$ ” in Fig. 4 and compared to the results during irradiation, where bands represent 1 standard deviation. We see that the two experiments fully overlap, indicating the small changes in frequency are likely to be caused by thermal drift.

We studied injection locking at 1x and 2x the STO frequency, which we refer to as 1f and 2f injection. The main result of this study is that the STO locking behavior is robust to gamma irradiation both in-situ and with respect to extreme total ionizing dose. Therefore, we confirm the MTJ based STO to be an excellent candidate for radiation hard neuromorphic computing applications.

Results of the 2f injection locking study are shown in Fig. 5. Fig. 5 (a)-(c), show example experimental data where  $I_{dc} = -0.47$  mA is fixed such that the free running STO frequency is  $f_{STO} \approx 0.55$  GHz. The injection frequency  $f_{inj}$  is swept and we find that the STO locks to the injection frequency in a certain range indicated by the vertical lines (vertical dashed lines indicate error in determining locking state). In this region,  $f_{STO} = 0.5 \cdot f_{inj}$  (indicated by sloped dotted line) and the amplitude of emission is increased (color tends towards red). We characterize the locking region by its central frequency and width (frequency distance between vertical lines). The results for all individual experiments are shown in Fig. 5 (d) and (e). Fig. 5 (d) shows results taken in the gamma chamber, while Fig. 5 (e) shows the 24 h experiment in the lab. We note a small drift in the center frequency of STO which we attribute to thermal drifts as it occurs in a similar fashion without the presence of gamma irradiation. We find that the locking region is robust to gamma irradiation as summarized in Fig. 5 (f), where the points indicate the mean locking width and error bars indicate 1 standard deviation. We see that within error, the 1f locking width does not change in the presence of gamma irradiation or after long exposure TID.

Results of the 1f injection locking study are shown in Fig. 6. Fig. 6 (a)-(c), show example experimental data where  $I_{dc} = -0.47$  mA is fixed such that the free running STO frequency is  $f_{STO}$

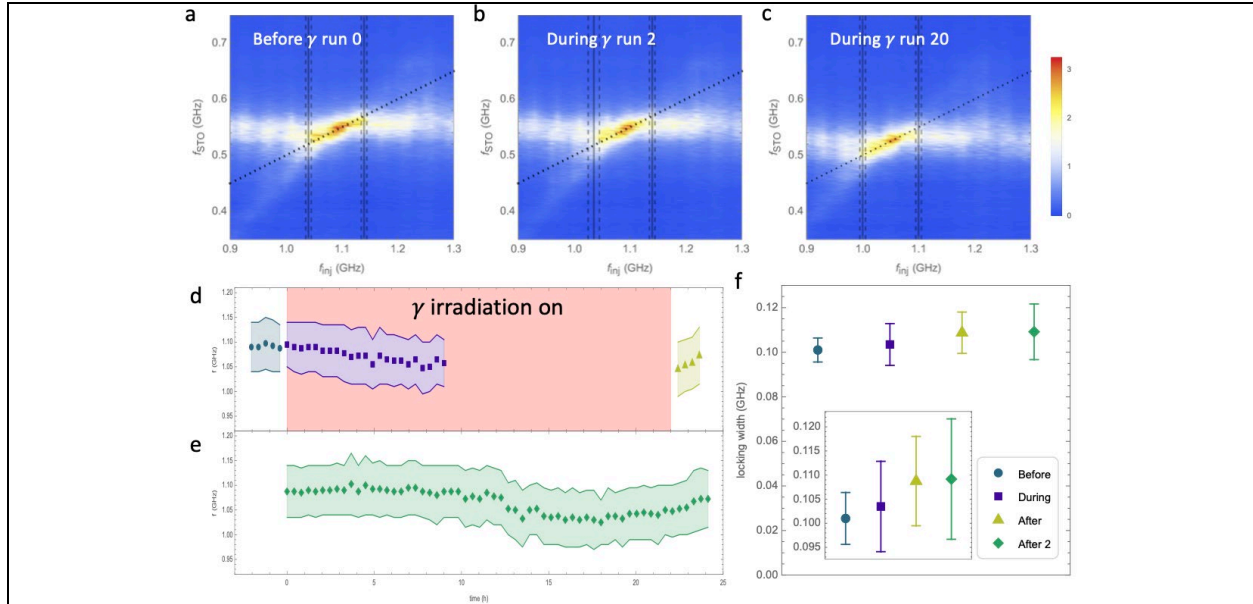


**Figure 5. 2f Injection locking of STO.** Example 2f injection locking for (a) before gamma irradiation and during gamma irradiation after (b)  $\sim 0.5$  h and (c)  $\sim 8$  h. Color scale indicates STO amplitude. Sloped dotted line indicates  $f_{inj} = 2 * f_{STO}$ . Vertical lines indicate the locking region where  $f_{STO} = 0.5 * f_{inj}$  and the amplitude of emission is increased. (d) Locking frequency center points (legend given in (f)) with bands indicating the locking region width. (e) Locking frequency center and width for 24 h measurement in lab after gamma irradiation. (f) Summary of mean locking width for each experiment with 1 standard deviation error bars.

$\approx 0.55$  GHz. The injection frequency  $f_{inj}$  is swept and we find that the STO locks to the injection frequency in a certain range indicated by the vertical lines (vertical dashed lines indicate error in determining locking state). In this region,  $f_{STO} = f_{inj}$ . Note that in this case, the direct signal from the injected microwave drive is detected as evident from the sloped red line representing clipped amplitude in colormap. We develop an algorithm to detect the locking region and characterize it by its central frequency and width (frequency distance between vertical lines). The results for all individual experiments are shown in Fig. 6 (d) and (e). Fig. 6 (d) shows results taken in the gamma chamber, while Fig. 6 (e) shows the 24 h experiment in the lab. We find a smaller drift for the 1f injection in comparison to the 2f injection locking. We find that the locking region is robust to gamma irradiation as summarized in Fig. 6 (f), where the points indicate the mean locking width and error bars indicate 1 standard deviation. We see that within error, the 1f locking width does not change in the presence of gamma irradiation or after long exposure TID.

The results shown in Figs. 5 and 6, demonstrate that the locking of MTJ STOs to external signals at either 1x or 2x the frequency  $f_{STO}$ . This is the key physical phenomena required for the implementation of STOs for spintronic neuromorphic computing applications. We show that the STO locking is unchanged both in the presence of gamma irradiation and to severe total ionization dose (TID =  $\sim 26$  kGy (2.6 Mrad) [silica]). Thus, our work during this period demonstrates that MTJ base STOs are compelling building blocks for radiation hard neuromorphic computing applications.

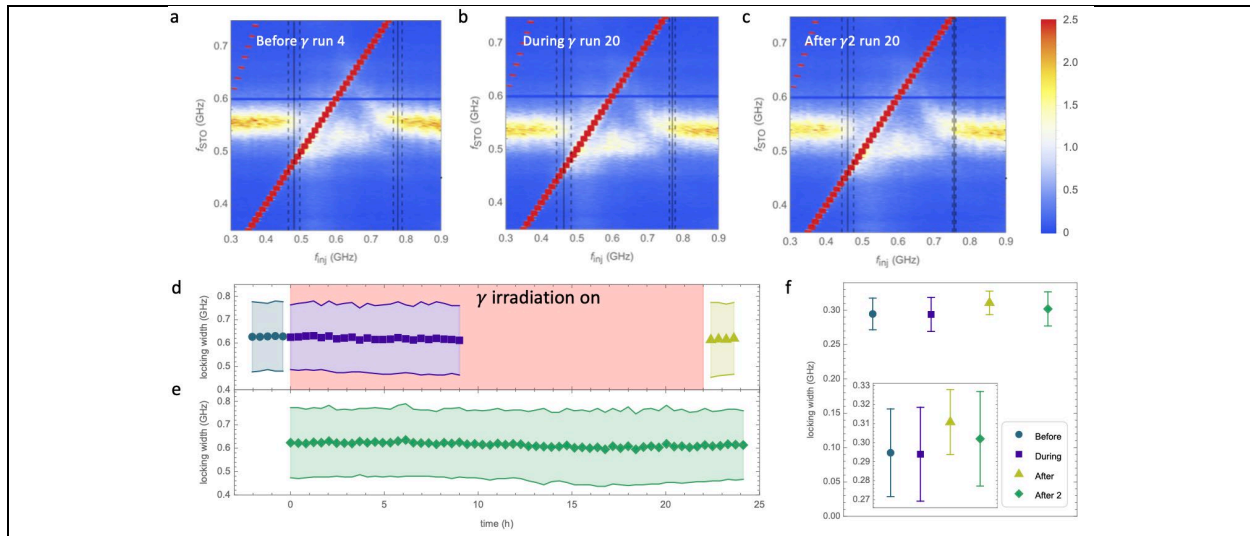


**Figure 6. 1f Injection locking of STO.** Example 1f injection locking for (a) before gamma irradiation, (b) during gamma irradiation after  $\sim 8$  h and (c) after irradiation in the lab after continuous experiment running  $\sim 8$  h. Color scale indicates STO amplitude. Vertical lines indicate the locking region where  $f_{STO} = f_{inj}$  and the amplitude of emission is increased. (d) Locking frequency center points (legend given in (f)) with bands indicating the locking region width. (e) Locking frequency center and width for 24 h measurement in lab after gamma irradiation. (f) Summary of mean locking width for each experiment with 1 standard deviation error bars.

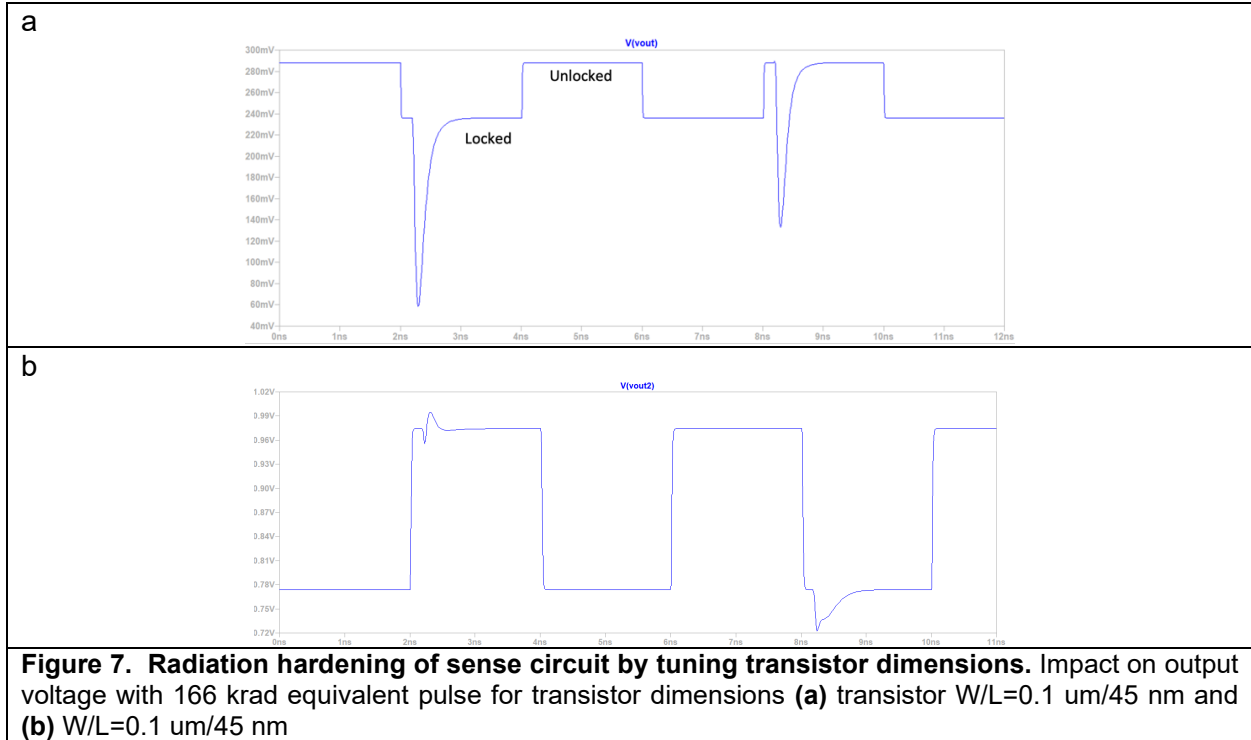
## Simulation of MTJ STO circuits

### Radiation hardening of MTJ STO CMOS sense circuit

In addition to experiment showing radiation hardness of MTJ STOs, we have studied the radiation hardening of the CMOS sense circuit. According to the previous simulations, the read-out circuit's output signal is affected by ionization equivalent to a pulse current of  $\sim 4.0$  fC, the equivalent of  $\sim 66$  krad dose. For this portion of the project, we identified that the impact of radiation induced charge current pulse could be mitigated by changing the transistor dimensions.

Fig. 7 (a) shows the ionization impact on the output signal when current pulse equivalent to 166 krad radiation was applied to the original CMOS circuit. In this case, the current pulse leads to significant changes to the output voltage and therefore error in detecting the locked/unlocked state of the STO. The proposed solution is to reduce this effect by changing the transistors' dimension. After adding a gain stage to the sense circuit and changing the width/length (W/L) ratio of the transistors the effect of ionization on the output is decreased. Figure 7 (b) shows the ionization impact with the new parameters.

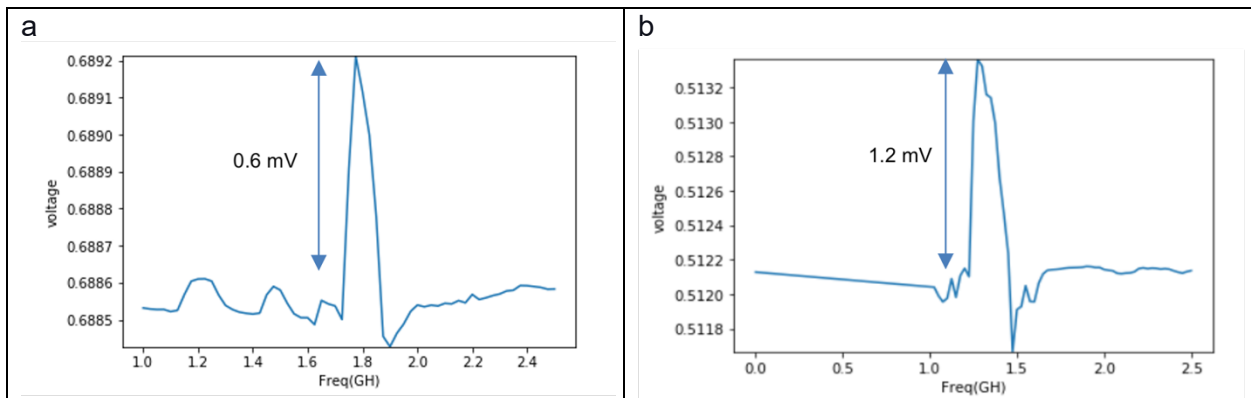
In this experiment, we reduced the ionization effect on the output signal by increasing the transistors' W/L ratio. According to simulations, by increasing the W/L of the transistors, we could achieve acceptable output for the 166.6 krad, 200 krad, 300 krad, and 400 krad radiation, and the locking and unlocking states are detectable from the output voltage.



### Spin diode effect for quasi-single domain MTJ STOs

The spin diode effect occurs when the frequency of AC input applied to the STO is the same as STO's natural frequency. In this situation, the DC voltage across the STO increases. M. Romera, et al, Nature **563**, 230 (2018) studied the spin diode effect in the vortex oscillators and used this effect for a neural network application. It proposed a detection circuit to detect the locking region of STO with the AC input via the spin diode effect. We implement a similar detection circuit to measure the DC voltage change that occurs in the locking region for the quasi-single domain free layer MTJs instead of vortex oscillators.

For the first step, we considered one STO along with AC injection input and measured the STO's DC voltage change in the locking region by the sense circuit. Fig. 8 (a) shows the circuit's output voltage for one STO when the applied DC current to the STO is  $I_{dc} = 1.0$  mA. The STO and the



AC input are locked at the 1.8 GHz, and the DC voltage in the locking region is increased 0.6 mV compared to the DC voltage in the nonlocking region. We repeated the simulation with  $I_{dc} = 1.6$  mA, and we obtained another locking region for STO as expected, as shown in Fig. 8 (b). This result shows that we can detect the locking regions by measuring the DC voltage of STO since the DC value will increase in the locking region.

For the next step, we connected four STOs in the series using the circuit shown in Fig. 9 (b). Each STO has a sense circuit that compares the STO DC voltage to the DC voltage of fixed resistor. For example, Fig. 10 shows the sense circuit's output  $V_{out}$  for STO2 as a function of input signal frequency. When STO2 locks to the input signal, there is a sharp DC voltage increase in  $V_{out}$ . Each of the four STOs in series will be locked with a different frequency of input, and the locking region can be detected by changes in the DC voltage of the sense circuit.

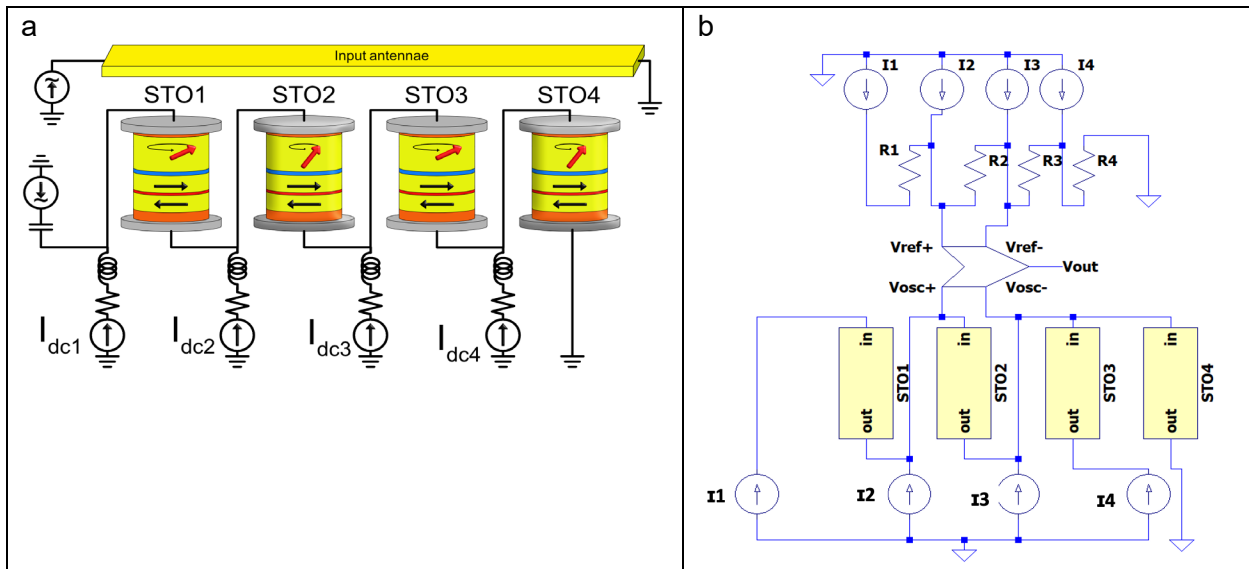


**Figure 9. Schematics for four STO circuit. (a)** Four STOs connected in series. **(b)** Sense circuit connected to STO2.

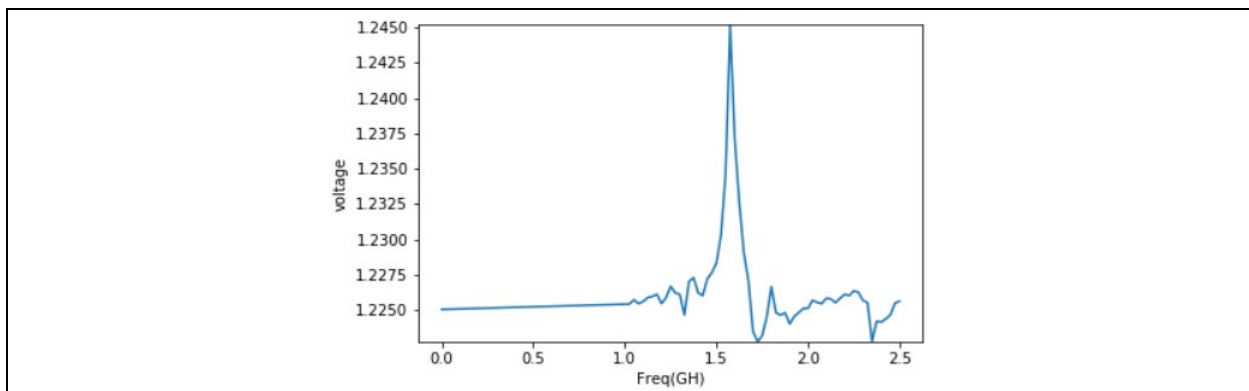


**Figure 10. A DC voltage of STO2 among the four series STOs, locking range is 1.6 GHz.**

## Opto-electric readout of STT-MRAM cells

In the previous review period, we worked on modeling of a parallel opto-electronic readout scheme for STT-RAM cells, where a pulsed laser beam illuminated an array of STT-RAM cells, inducing a voltage across each cell through optical rectification effect, further enhanced by plasmonic resonance (Fig. 11).

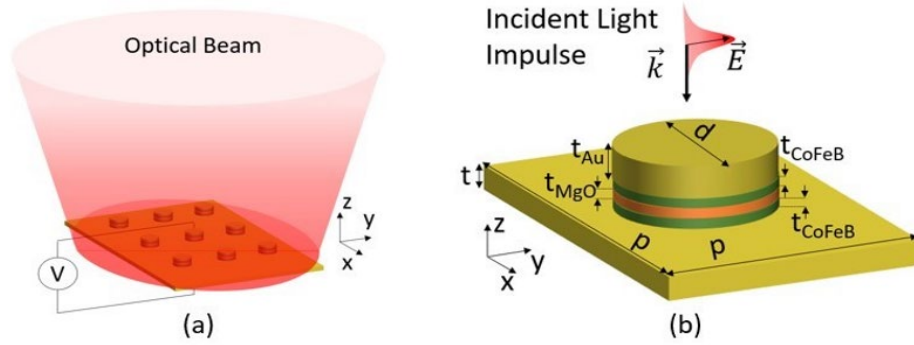


**Figure 11.** (a) Schematic of the proposed optoelectronic readout method for STT-RAM array (b) Unit cell geometry of STT-RAM array

During the current review period, we continue studying such readout method, where we have focused on optimization of the STT-RAM dimensions to achieve a higher memory readout speed. To do so, we have performed in-depth study of the effect of STT-RAM dimensions on the readout speed. Details of such study are discussed in our paper, to be submitted shortly [2]. Further increase of the readout speed can be performed via increasing the incident peak power. Therefore, we increase the incident peak power to 3 kW, which is still in the practical range for pulsed lasers. With these modifications, and based on our calculation model, which was previously explained, our calculation shows that a memory readout speed of up to  $\sim 300$  Gbit/sec can be achieved (STT-RAM array dimensions  $p=200\text{nm}$ ,  $d=100\text{nm}$ ,  $t_{\text{Au}}=105\text{nm}$ ,  $t_{\text{CoFeB}}=0.9\text{nm}$ ,  $t_{\text{MgO}}=2\text{nm}$ ,  $t=100\text{nm}$ , incident peak power of 3 kW and illumination beam spot size of  $20\mu\text{m}\times 20\mu\text{m}$ ,  $\text{SNR} = 3 \text{ dB}$ ,  $\text{NEP} = 4 \text{ nV}/\sqrt{\text{Hz}}$ ).

After performing the optimization of the STT-RAM array, we evaluate the impact of transparent electrodes that will couple the  $V_{\text{OR}}$  to the rest of the electrical circuitry. The photonics part of the design is especially interested in the impact of electrodes made of materials like ITO placed on top of the Au nanodisc in the unit cell structure as shown in Fig. 12(a). The space between the ITO layer and the Au plane at the bottom of the memory cell is filled with  $\text{SiO}_2$  to support the ITO layer. Looking at the absorption spectrum of the structure and comparing it with the previous case where no ITO and  $\text{SiO}_2$  are present (blue curves in Fig. 12(b)), a 30% increase in absorption peak is calculated, which means a stronger plasmonic resonance. This in turn increases the field localization around the MgO layer, and results in further enhancement in the memory readout rate. As it can be seen in Fig. 12(b), the maximum readout rate provided by this structure is  $\sim 527 \text{ Gbit/s}$ , which is  $\sim 75\%$  larger than the case without ITO and  $\text{SiO}_2$ . Through further investigation of the data (results not included here), we have verified that such enhancement is mainly due to the added  $\text{SiO}_2$  around the memory cell, and the ITO layer has a minor effect, which

is due to its small absorption. We note that the plasmonic enhancement of the readout rate in this case is more than 400 times compared to the off-resonance wavelength of 1.3  $\mu\text{m}$ .

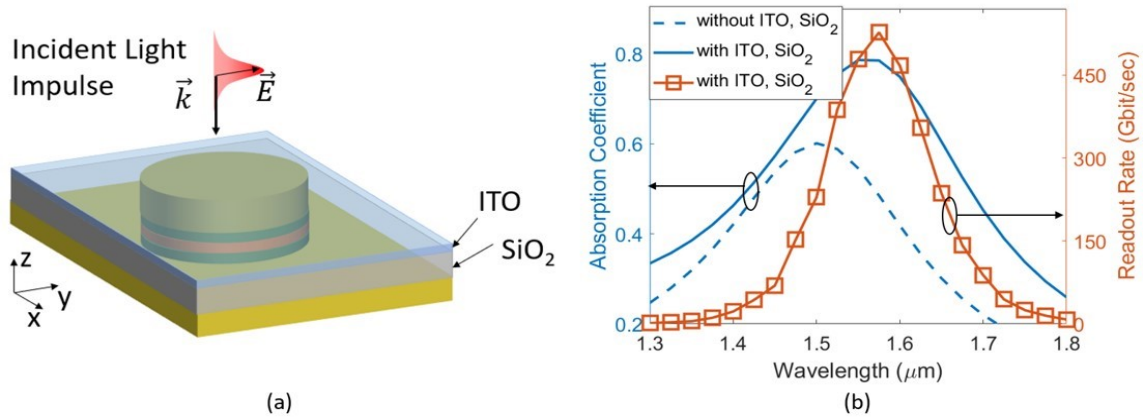


**Figure 12.** (a) Schematic of STT-RAM array unit cell with added ITO electrode and SiO<sub>2</sub> (b) Absorption coefficient of the STT-RAM array with and without ITO and SiO<sub>2</sub> and the memory readout rate of the one with ITO and SiO<sub>2</sub> (STT-RAM array dimensions  $p=200\text{nm}$ ,  $d=100\text{nm}$ ,  $t_{\text{Au}}=105\text{nm}$ ,  $t_{\text{CoFeB}}=0.9\text{nm}$ ,  $t_{\text{MgO}}=2\text{nm}$ ,  $t=100\text{nm}$ ,  $t_{\text{ITO}}=10\text{nm}$ , incident peak power of 3 kW and illumination beam spot size of  $20\mu\text{m}\times 20\mu\text{m}$ , SNR = 3 dB, NEP = 4 nV/ $\sqrt{\text{Hz}}$ ).

**What opportunities for training and professional development has the project provided?**

*If the research is not intended to provide training and professional development opportunities or there is nothing significant to report during this reporting period, state "Nothing to Report." Describe opportunities for training and professional development provided to anyone who worked on the project or anyone who was involved in the activities supported by the project. "Training" activities are those in which individuals with advanced professional skills and experience assist others in attaining greater proficiency. Training activities may include, for example, courses or one-on-one work with a mentor. "Professional development" activities result in increased knowledge or skill in one's area of expertise and may include workshops, conferences, seminars, study groups, and individual study. Include participation in conferences, workshops, and seminars not listed under major activities.*

One PostDoc (Eric Montoya) was invited to give an invited talk at IEEE International Conference on "Nanomaterials: Applications & Properties", Odessa Ukraine, November 2020

### How have the results been disseminated to communities of interest?

*If there is nothing significant to report during this reporting period, state "Nothing to Report."*

*Describe how the results have been disseminated to communities of interest. Include any outreach activities that have been undertaken to reach members of communities who are not usually aware of these research activities, for the purpose of enhancing public understanding and increasing interest in learning and careers in science, technology, and the humanities.*

DTRA acknowledged journal papers:

1. Etesamirad, R. Rodriguez, J. Bocanegra, R. Verba, J. Katine, I. N. Krivorotov, V. Tyberkevych, B. Ivanov, and I. Barsukov, *Controlling Magnon Interaction by a Nanoscale Switch*, ACS Appl. Mater. Interfaces **13**, 20288 (2021).
2. J.-R. Chen, P. Lam Tse, I. N. Krivorotov, and J. G. Lu, *Spin–Momentum Locking Induced Non-Local Voltage in Topological Insulator Nanowire*, Nanoscale **12**, 22958 (2020).
3. J.-R. Chen, A. Smith, E. A. Montoya, J. G. Lu, and I. N. Krivorotov, *Spin–Orbit Torque Nano-Oscillator with Giant Magnetoresistance Readout*, Commun Phys **3**, 1 (2020).
4. P. Sadri-Moshkenani, M. W. Khan, M. S. Islam, E. Montoya, I. Krivorotov, and O. Boyraz. *High-Speed Optoelectronic Readout of STT-RAM Based on Plasmon Drag Effect.*, Submitted and pending review in IEEE Journal of Quantum Electronics, 2021.

DTRA acknowledged conference papers:

1. P. Sadri-Moshkenani, M. W. Khan, M. S. Islam, D. Shi, E. Montoya, I. Krivorotov, N. Bagherzadeh, and O. Boyraz. *Optoelectronic Readout of STT-RAM Memory Cells Using Plasmon Drag Effect In CLEO: Fundamental Science*, pp. JTu3A.69. Optical Society of America, 2021.

Conference and Seminar Presentations:

1. E. A. Montoya, *Magnetization reversal driven by low dimensional chaos in a nanoscale ferromagnet*, IEEE International Conference on Nanomaterials: Application & Properties (NAP-2020), Odesa, Ukraine (**Invited Talk**, virtual)